Materials Advances

ROYAL SOCIETY OF CHEMISTRY

PAPER

View Article Online
View Journal | View Issue

Cite this: *Mater. Adv.*, 2025, 6, 3730

Phyto-mechanochemical synthesis of an Ag@GO/CNT catalyst: enhanced hydrogen production *via* a continuous flow system†

Fatimah AlSulami,[a] Merfat M. Alsabban,[a] Hadeel M. Banbela,[b] Noushi Zaidi,[cd] Sadaf Habib,[e] Dina Hajjar,[f] Arwa A Makki,[f] Ismat Bibi,[e] Tariq Javed,[g] Aysha Afzal[e] and Muhammad Babar Taj *[e]

Due to its high energy density and minimal emissions, hydrogen is a promising alternative energy source. For sustainable development, hydrogen production from non-fossil sources is essential. The hydrolysis of sodium borohydride enables rapid hydrogen production on demand, particularly with the aid of a catalyst. Thus, developing efficient and cost-effective catalysts for this process is essential. Herein, a phyto-mechanochemical approach is employed to obtain a material containing silver (Ag), reduced graphene oxide (rGO), and multi-walled carbon nanotubes (MWCNTs) for use as a high-performance H_2 production catalyst at room temperature *via* the water displacement method. All the samples (Ag NPs, Ag@rGO, and Ag@rGO/CNT) were characterized by ultraviolet-visible spectroscopy, Fourier-transform infrared spectroscopy, scanning electron microscopy, and X-ray diffraction. The morphological analysis confirmed the presence of mechanochemical Ag NPs uniformly dispersed on the rGO and CNTs. The results revealed that Ag@rGO/CNT exhibited superior particle distribution and porosity characteristics, achieving a high hydrogen generation rate of 4243 mL min^{-1} g_{cat}^{-1}. The activation energy for the sodium borohydride hydrolysis reaction on the Ag@rGO/CNT catalyst was determined to be 7.08 kJ mol^{-1}, as calculated using the Arrhenius equation and the zero-order reaction model. The catalyst's superior performance is confirmed by its low activation energy compared to Ag NPs and Ag@rGO catalysts. The results of the recycling experiments also showed that, after four repetitive cycles, the catalyst's performance gradually declined with each subsequent cycle. The Ag@rGO/CNT catalyst's previously listed characteristics make it an effective catalyst for the hydrolysis of $NaBH_4$, resulting in the production of hydrogen.

Received 13th February 2025,
Accepted 14th April 2025

DOI: 10.1039/d5ma00136f

rsc.li/materials-advances

1. Introduction

Due to industrialization and population growth, the world's energy demands and environmental impacts are increasing rapidly. To meet the energy needs of the rapidly expanding population, it is therefore highly desirable to develop alternative, clean, sustainable, and efficient energy sources. Because of its excellent energy capacity, cleanness, and environmental friendliness, hydrogen, without reservation, is the most promising renewable energy resource to replace fossil fuels.[1–3] Additionally, hydrogen, a zero-emission fuel, is utilized in proton exchange membrane fuel cells. About 95% of hydrogen is produced by gasifying coal, methane, and natural gas through high-temperature steam reforming.[4] Some additional methods for producing hydrogen include bio-hydrogen synthesis, water splitting or oxidation (*via* electrolysis, photocatalysis, and thermolysis), and the hydrolysis of hydrogen-holding materials (such as amines and hydrides).[5] Hydrogen is a "green" and sustainable energy source that lessens air pollution without emitting greenhouse gases.[6–9] Metal hydride's catalytic hydrolysis is thought to be the most promising, appropriate, economical, and potent technique for producing hydrogen out of all the ways mentioned.[10–12] Because of its high gravimetric capability (approximately 10.8 weight%), non-inflammability, non-toxic nature, and high stability in air, sodium borohydride is the

[a] *Department of Chemistry, College of Science, University of Jeddah, Jeddah 21959, Saudi Arabia*
[b] *Department of Chemistry, University of Jeddah, Jeddah, Saudi Arabia*
[c] *Department of Basic Sciences, Preparatory Year, King Faisal University, Al-Ahsa 31982, Saudi Arabia*
[d] *Department of Chemistry, College of Science, King Faisal University, Al-Ahsa 31982, Saudi Arabia*
[e] *Institute of Chemistry, The Islamia University of Bahawalpur, Bahawalpur, Pakistan. E-mail: dr.taj@iub.edu.pk*
[f] *Department of Biochemistry, College of Science, University of Jeddah, Jeddah, Saudi Arabia*
[g] *Department of Chemistry, University of Sahiwal, Sahiwal, Pakistan*

† Electronic supplementary information (ESI) available. See DOI: https://doi.org/10.1039/d5ma00136f

greatest examined metal hydride and a promising option for hydrolysis-based, on-demand hydrogen production with the right catalyst.[13–15]

Moreover, when sodium borohydride is hydrolyzed, the resulting by-product is only sodium metaborate ($NaBO_2$), which is safe for the environment and soluble in water.[16,17] To achieve high hydrogen production activity through sodium borohydride's hydrolysis, other catalysts studied on various supports[16,18] are Pd, Pt, Ru, Rh, and Ru–Pd–Pt.[16,19] However, the scarcity of noble metals and their high cost restrict their application in industrial environments. The energy supply is a critical global issue because of the depletion of fossil fuels and the need for high-performance energy systems.[20] Such systems must be portable, cost-effective, eco-friendly, and reproducible.[21,22] Several attempts have been made to meet the current energy demands due to globalization. Fuel cells and supercapacitors are required energy systems, and their performance directly depends on the properties of the materials used in their synthesis.

Advanced (metal) nanoparticles (NPs) now play an essential role in modern catalytic applications due to their interesting electrical and optical properties, namely, large surface area and the need for low loadings.[23] Despite having an efficient electronic configuration, the catalytic abilities of gold and silver metals are not optimal. However, their NPs exhibit surprisingly high catalytic behavior.[24] The green synthesis of silver nanoparticles (Ag NPs) is a recognized environmentally sustainable method.[25–29] Nature offers many plants, several of which have been utilized to synthesize Ag NPs.[30–34] The plants vary in their ability to reduce Ag^+ ions to Ag^0, a crucial step in the synthesis process. Integrating mechanochemistry with green synthesis, called phyto-mechanochemical synthesis, exhibits enhanced environmentally favorable characteristics.

It is well understood that supports enhance the NP's catalytic behavior by modifying their electronic properties.[35] Reduced graphene oxide (rGO) has proved to be the best support due to its extraordinary mechanical and electrical properties.[36] rGO is a combination of sp^3 and sp^2 carbon containing carboxyl, hydroxyl, and epoxy groups.[37,38]

Agglomeration between graphene sheets reduces the surface area and the number of catalytic active sites, adversely affecting the electrocatalytic strength. This problem can be overcome by combining carbon nanotubes (CNTs) with reduced graphene oxide (rGO). CNTs act as spacers between the rGO sheets.[39] They are a network of one-dimensional sp^2 hybridized carbon atoms. The morphology and electronic properties of CNTs and rGO make their combination a very efficient catalytic support. Catalytically active metal particles may be adsorbed on the exterior or interior of CNTs.[40] Initially, Pt-based catalysts were utilized, but their high cost diverted researchers' interest to other materials.[41]

In this study, we concentrate on the phyto-mechanochemical synthesis of silver nanoparticles (Ag NPs) and a silver-reduced graphene oxide (Ag@rGO) catalyst using extracts from *Polygonum acetosum*, a member of the *Polygonaceae* family commonly found in temperate regions. We have identified the presence of this plant near the Afghan border in Pakistan. Notably, it has not been previously used to synthesize Ag NPs or Ag@rGO. The synthesized Ag@rGO was further fabricated with CNTs to form an Ag@rGO/CNT catalyst. Hydrolyzing $NaBH_4$ in a continuous flow system using the water displacement method, the potential of each sample to produce hydrogen is ascertained. To the best of our knowledge, the phyto-mechanochemical synthesis of the Ag@rGO/CNT catalyst and its comparative study in $NaBH_4$ hydrolysis have not been published.

2. Materials and methods

2.1. Materials

Graphite powder (<45 μm, ≥99.99%), sodium nitrate (99.0%), multiwalled carbon nanotubes (>98%), sulphuric acid (99.99%), potassium manganate (99.0%), silver nitrate (99.99%), hydrogen peroxide (30% (w/w) in H_2O), hydrochloric acid (37%), and sodium borohydride ($NaBH_4$) were purchased from Sigma Aldrich. Chemicals were used without pretreatment. Double-distilled water was used in all experiments.

2.2. Phyto-mechanochemical synthesis of Ag@rGO/CNT

Phyto-mechanochemical synthesis is recognized as a compelling alternative to traditional methods for preparing nanocrystalline materials, such as silver nanoparticles. Nevertheless, applying phyto-mechanochemical methods for manufacturing Ag NPs utilizing natural resources remains a largely uncharted domain.

1st step: the *Polygonum acetosum* plant extract was prepared by crushing the plant leaves in a mortar and pestle and squeezing to obtain 20 mL of extract. In a separate beaker, 10 mL of extract was mixed with 0.1 g of $AgNO_3$. The mixture was then milled in a planetary ball mill[42] (details are given in the ESI†). The product was washed with water multiple times. The Ag NPs were collected using centrifugation.

2nd step: for the Ag@rGO sample, GO was initially synthesized from graphite flakes by the modified Hummers' method.[43] Then, $AgNO_3$ and GO were mixed in an equal mol% ratio with 20 mL of plant extract and milled in a planetary ball mill. The process was repeated, and the product was labeled as Ag@rGO NPs. Alone, rGO was also synthesized using the same phyto-mechanochemical method without $AgNO_3$ salt.

3rd step: Ag@rGO/CNT was prepared by mixing 10 mL of freshly prepared Ag@rGO (3.0 mg mL^{-1}) with 10 mL of CNT under stirring for 30 min, followed by sonication for 2 h. The reaction mixture was centrifuged, dried, and ground into a fine powder.

2.3. Characterization

Information about the electronic transitions of the prepared samples was obtained using UV-vis spectroscopy (with a Cecil 7500 UV-vis spectrophotometer) within a range of 200 cm^{-1} to 800 cm^{-1}. A Fourier transform infrared spectrophotometer (Bruker Tensor 27 FT-IR, operating in the range of 400 cm^{-1} to 4000 cm^{-1}) was used to analyze the functional groups. A powder X-ray diffractometer (Bruker D8 Advance PXRD with a

Cu radiation source and a Lynx Eye detector were utilized to obtain information about the analyte's crystal structure and particle size. A scanning electron microscope (MIRA-III TESCON) was employed to study surface morphology and particle size. To measure the surface area and pore size distribution of the manufactured samples, nitrogen was physically adsorbed onto the catalyst surface over a range of relative pressures from 0.05 to 0.99. The analysis was carried out using a Japanese Belsorp gadget.

2.4. Hydrogen production measurement

A hydrolysis reaction was carried out in a continuous system[12] to ascertain the hydrogen generation rate. 25 mg of catalyst was initially injected into a two-neck flask, which served as a reactor at a constant temperature of 25 °C. The glass reactor was then filled with 5 mL of an aqueous solution containing 50 mg $NaBH_4$ (0.27 M) at a flow rate of 30 mL h^{-1} using a Terufusion Syringe Pump, model STC 523. During a batch process, 50 mg of $NaBH_4$ and 25 mg of catalyst were kept at the bottom of a conical flask on a magnetic stirrer. The burette was linked to the reaction flask, which was securely sealed with a septum to regulate water flow. The only difference between these two approaches was that the continuously stirred tank reactor used a syringe pump with a preset flow rate of $NaBH_4$ rather than a standard burette to drop the water into the catalyst and $NaBH_4$ mixture (Batch process). Fig. S1 and S2 (ESI†) depict the experimental configurations for producing H_2 from the hydrolysis of $NaBH_4$ in a continuous system and batch system, respectively. As soon as the reaction began, H_2 evolution commenced, and the amount of hydrogen produced was measured by observing the displacement of the water level in the nearby vacuum Erlenmeyer flask. According to published research, the catalyst quantity (measured in millilitres per minute × g_{cat} unit) and the maximum amount of hydrogen produced per reaction time are used to calculate the hydrogen generation rate (HGR). The average outcomes of each experiment were reported after it was carried out at least three times. After the reaction, the catalyst was thoroughly cleaned with ethanol and water and dried at 100 °C. Under the same experimental circumstances, this catalyst was utilized again.

3. Results and discussion

3.1. Phytochemical investigation

The plant leaf extract had negative results for steroids but good results for glycosides, alkaloids, saponins, flavonoids, terpenoids, anthraquinones, and tannins (Table 1).[43,44]

A comparison of the phyto-mechanochemical method with an existing process for synthesizing Ag-based nanocomposites is presented in Table 2.

3.2. UV-vis analysis

UV-vis spectroscopy was used to study the optical properties of the prepared samples. The obtained spectra are presented in Fig. 1. The peak indicates the formation of silver nanoparticles at 440 nm. The absorption range of 400–500 nm in UV-visible spectroscopy is characteristic of AgNPs due to a phenomenon known as localized surface plasmon resonance (LSPR). Plasmons are collective oscillations of free electrons in a metal

Table 1 Phytochemicals in a leaf extract of *Polygonum acetosum*

Phytochemical type	Test	Observation	Result
Glycosides	Keller Killiani	The lower reddish-brown layer & upper acetic acid layer turn bluish green	+
Alkaloids	Dragendorff's	Turbidity/precipitation	+
Saponins	Froth	Stable froth formation and emulsion formation after olive oil	+
Flavonoids	Ferric chloride	Formation of yellow colour, which changed to colorless on acid addition	+
Terpenoids	Liebermann Burchard	The appearance of reddish brown-deep, red color	+
Anthraquinones	Bontrager's	The appearance of pink in the aqueous layer	+
Tannins	Gelatin	The appearance of a white precipitate	+
Steroids	Liebermann Burchard	The green-to-pink color was absent	−

+: phytochemical present, −: phytochemical absent.

Table 2 Comparative analysis of the phyto-mechanochemical method with previously published methods

Method	Key characteristics	Advantages	Disadvantages
Phyto-mechanochemical synthesis[45]	Uses plant extracts for green synthesis + ball milling/mechanical activation	Eco-friendly (no toxic chemicals), simultaneous reduction & stabilization, cost-effective, avoids harsh conditions	Limited control over particle size, dependent on phytochemical composition
Chemical reduction[46]	Uses reducing agents (*e.g.*, $NaBH_4$, hydrazine) to deposit Ag on rGO/CNT	High control over size and dispersion scalable	Uses toxic chemicals, requires multiple washing steps
Electrochemical deposition[47]	Electrochemical reduction of Ag^+ onto rGO/CNT in an electrolyte	Good particle distribution Precise control over deposition	Requires specialized equipment, time-consuming
Solvothermal/ hydrothermal[48]	Uses high-temperature, high-pressure synthesis in an autoclave	High crystallinity, strong adhesion of Ag to rGO/CNT	Requires high energy, long processing time
Microwave-assisted synthesis[49]	Uses microwaves to reduce Ag onto rGO/CNT rapidly	Fast synthesis energy-efficient	Requires optimized conditions to prevent aggregation
UV-assisted photoreduction[50,51]	Uses UV light to excite electrons for Ag^+ reduction on rGO/CNT	No harsh chemicals, uniform deposition	Requires UV source, may have low yield

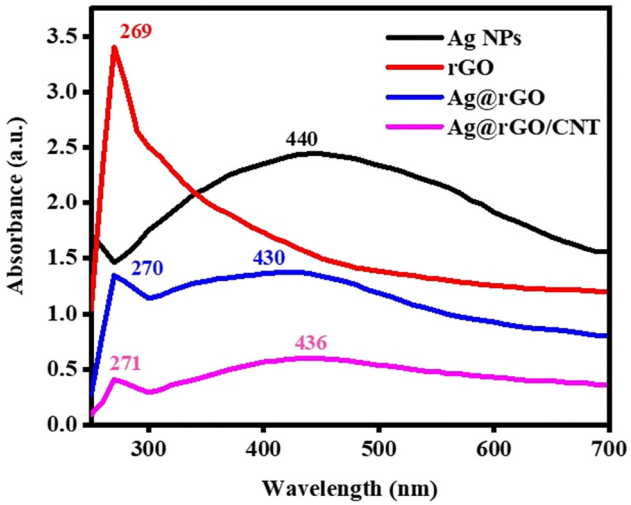

Fig. 1 UV-vis spectrum of Ag NPs, rGO, Ag/rGO, and the Ag@rGO/CNT catalyst.

nanoparticle, such as silver, that occur when the nanoparticle is exposed to electromagnetic radiation, commonly referred to as light. When light interacts with a metal nanoparticle, the electrons at the particle's surface oscillate collectively in resonance with the incident light. This phenomenon is known as localized surface plasmon resonance (LSPR). The LSPR effect is susceptible to the size, shape, and environment of the nanoparticle, as well as the wavelength of the incident light. Ag NPs have free conduction electrons that can oscillate in response to electromagnetic radiation, including light. At specific wavelengths, the collective oscillation of these electrons, known as the plasmon, is resonant with the frequency of the incoming light. This leads to enhanced absorption of light at specific wavelengths. For Ag NPs, LSPR typically occurs in the visible region of the electromagnetic spectrum, at wavelengths ranging from 400 to 500 nm, where the conduction electrons in the Ag NPs oscillate collectively in response to incident light. This absorption is strongly dependent on the particle size, shape, and surrounding environment, and for Ag NPs, it typically occurs within this range due to their intrinsic electronic properties.[42] Shifting to higher wavelength values suggests the formation of Ag NPs of larger sizes.[52] In the spectrum of rGO, the π–π* transitions of C═C appeared at 269 nm, while the absence of a C═O shoulder peak (n–π* transition) at 284 nm confirmed the presence of rGO. In Ag@rGO, the presence of Ag NPs and rGO is confirmed by the 430 nm and 270 nm peaks, respectively.[53]

3.3. FT-IR analysis

FT-IR analysis of the samples is depicted in Fig. 2. The FT-IR spectrum of the Ag NPs showed a peak at 1032 cm^{-1}, indicative of specific functional groups from the biological entities used in their synthesis. This peak is commonly associated with C–O stretching vibrations of alcohols and glycosides or C–N stretching vibrations of aliphatic amines, suggesting the involvement of these groups in the reduction and stabilization processes of the AgNPs.[54] For instance, a study on the biosynthesis of Ag NPs

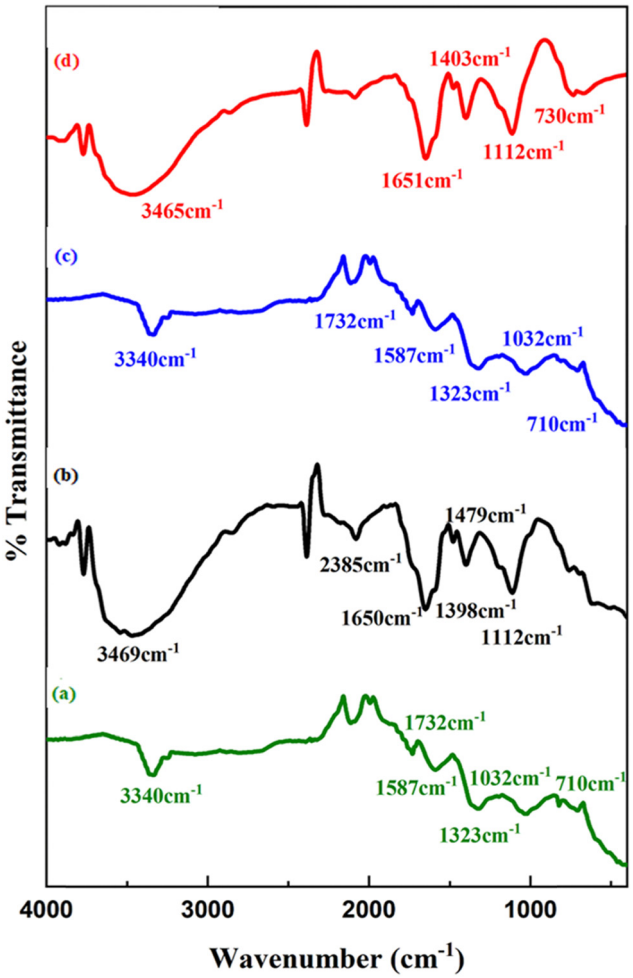

Fig. 2 FT-IR spectrum of (a) Ag NPs, (b) rGO, (c) Ag@rGO, and (d) Ag@rGO/CNT.

using *Cassia auriculata* flower extract reported an FTIR peak at 1032 cm^{-1}, attributed to C–N stretching vibrations, which highlights the role of amine groups in nanoparticle stabilization. Similarly, research involving *Sargassum wightii* seaweed extract observed a peak at 1032 cm^{-1} in the FTIR spectrum of the extract, corresponding to C–N stretching vibrations of aliphatic amines, which are implicated in the capping of NPs.[55,56] A band at 3340 cm^{-1} is attributed to a hydroxyl group, while a peak at 824 cm^{-1} is often associated with C═C and C–H stretching vibrations in the hydrocarbon portions of biomolecules.[57] The peak around 710 cm^{-1} is relatively uncommon. It could be associated with C–H bending vibrations of aromatic compounds or out-of-plane bending in substituted benzene derivatives. Typically, C–H bending vibrations occur at approximately 750 cm^{-1}.[58] A minor peak at 823 cm^{-1} corresponds to Ag–O due to the small amount of Ag_2O NPs.[59] The stretching hydroxyl group peak, observed at 3469 cm^{-1}, confirmed the presence of hydroxyl groups at the edges of rGO, a range typically observed between 3500 cm^{-1} and 3000 cm^{-1}. Oxygenated functional moieties exhibited peaks at 1650 cm^{-1}, 1479 cm^{-1} (carboxyl groups), and 1112 cm^{-1} (alkoxyl groups).[60] Other peaks are

attributed to the metabolites of *Polygonum acetosum*.[61] The carbonyl groups in the Ag@rGO catalyst are responsible for the peak at 1732 cm^{-1} in the FT-IR spectra.[62]

3.4. XRD analysis

The XRD diffractograms are displayed in Fig. 3. The peaks of Ag NPs at 2θ angles of 38.2°, 44.5°, 64.8°, and 77.7° in Fig. 3a correspond to the 111, 200, 220, and 311 planes, respectively, indicating the presence of silver nanoparticles in the face-centered cubic crystalline phase (JCPDS 00-004-0783).[63] The crystallite size of the Ag NPs was 6.93 nm, as calculated by the Scherrer equation.[64] The XRD peaks confirm the presence of rGO at 25.48° (002), as shown in Fig. 3b.[65] In terms of the Ag@rGO nanocomposite shown in Fig. 3c, the additional peaks confirm the presence of Ag NPs at 38.2°, 44.5°, 64.8°, and 77.7°, corresponding to the 111, 200, 220, and 311 planes, respectively. The crystallite size is 9.60 nm, as estimated by the Scherrer equation. The diffractogram also proved the absence of impurities in the catalyst.

In comparison to the (002) peaks in Fig. 3b and c, a slight right shift is observed. However, it is commonly observed that the incorporation of Ag NPs into rGO leads to a right shift (particularly in the (002) plane of rGO), indicating a decrease in interlayer spacing.[66] Upon incorporating CNTs, the diffraction peaks varied slightly depending on the CNT loading. In our case, a small amount of CNT loading resulted in a further decrease in *d*-spacing, as the graphene sheets were further straightened and aligned, and the (002) peak slightly shifted to the right.[67]

In the Ag@rGO/CNT nanocomposite portrayed in Fig. 3d, the peaks at 38.2° (111), 45.93° (200), 64.8° (220), and 77.7° (311) confirmed the presence of Ag NPs. The peaks at 25.89° (002) and 42.78° (100) indicated the presence of CNTs. In the Ag@rGO/CNT catalyst, the peak position of the 200 plane of the Ag NPs shifted towards a higher 2θ due to the strain value generated at the Ag–CNT interface during ultrasonic treatment.[68] The Scherrer equation gives a crystallite size value of 8.40 nm for the Ag@rGO/CNT catalyst.

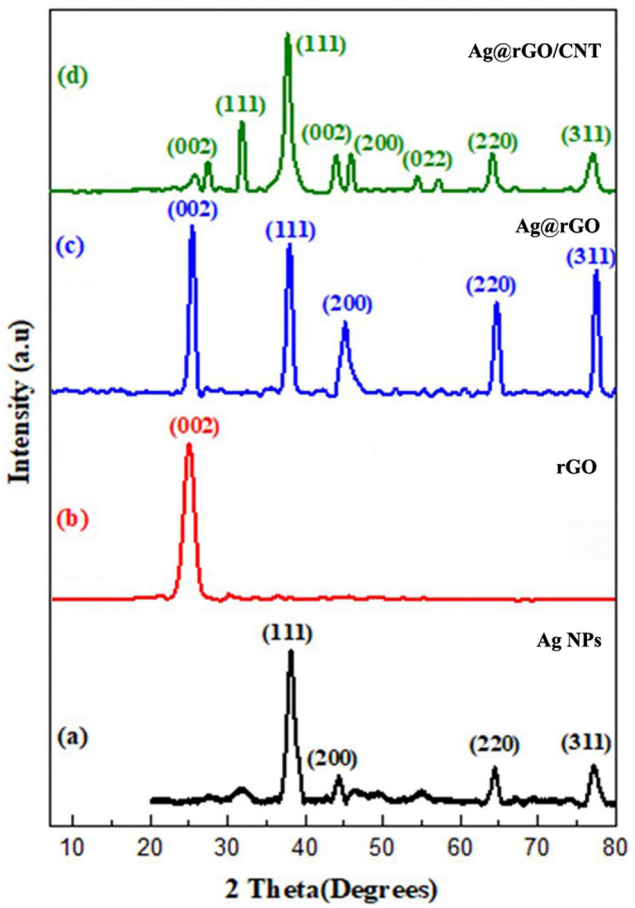

Fig. 3 PXRD diffractograms of (a) Ag NPs, (b) rGO, (c) Ag@rGO, and (d) Ag@rGO/CNT.

3.5. SEM analysis

SEM characterizations were employed to investigate the morphology of the samples. The SEM image of Ag (Fig. 4a) showed a spherical shape for the Ag NPs, with a grain size of 3.34 μm. Fig. 4b shows the SEM image of rGO, which confirms its layered morphology. The SEM image of the Ag@GO nanocomposite confirms the presence of Ag NPs on graphene oxide layers, as shown in Fig. 4c. Herein, Ag NPs are agglomerated. The SEM image of the Ag@rGO/CNT nanocomposite depicted in Fig. 4d revealed the presence of a rod-like structure, which confirmed the presence of CNTs.[61] The EDX mapping (Fig. 4d) justifies the elemental composition of Ag@GO/CNT.

3.6. N_2 adsorption/desorption analysis

The BET technique was used to determine the pore characteristics of the catalysts. This technique determines surface area and pore volume by analysing nitrogen gas surface adsorption and desorption isotherms. As illustrated in Fig. 5, AgNPs have a surface area of 11.35 $m^2\ g^{-1}$ and a pore volume of 0.09 mL g^{-1}, whereas Ag@rGO has a surface area of 25.79 $m^2\ g^{-1}$ and a pore volume of 0.19 mL g^{-1}. After injection, CNTs may interact with the support surface through diffusion into the support matrix, chemical bonding, or physical adsorption. These interactions may lead to a novel phase or structure at the interface between CNTs and Ag@rGO, thereby improving the pore properties (surface area: 32.65 $m^2\ g^{-1}$ and pore volume: 0.32 mL g^{-1}). An increase in surface area gives reactant molecules access to more active sites. Therefore, the Ag@rGO/CNT sample is expected to perform better in sodium borohydride hydrolysis.

3.7. Comparison of $NaBH_4$ as a H_2 source to other H_2 sources

Sodium borohydride ($NaBH_4$) offers several advantages as a source of hydrogen (H_2) compared to other reported sources. Firstly, $NaBH_4$ has a theoretical hydrogen content of 10.8 wt%, which is higher than that of many other hydrogen storage materials.[69] Also, the hydrolysis of $NaBH_4$ is exothermic and can occur at room temperature, enabling on-demand hydrogen generation without requiring external energy input. This reaction is typically catalyzed by metals or metal composites, ensuring a controlled and safe release of hydrogen.[69] $NaBH_4$ is also stable under dry conditions and can be safely stored for

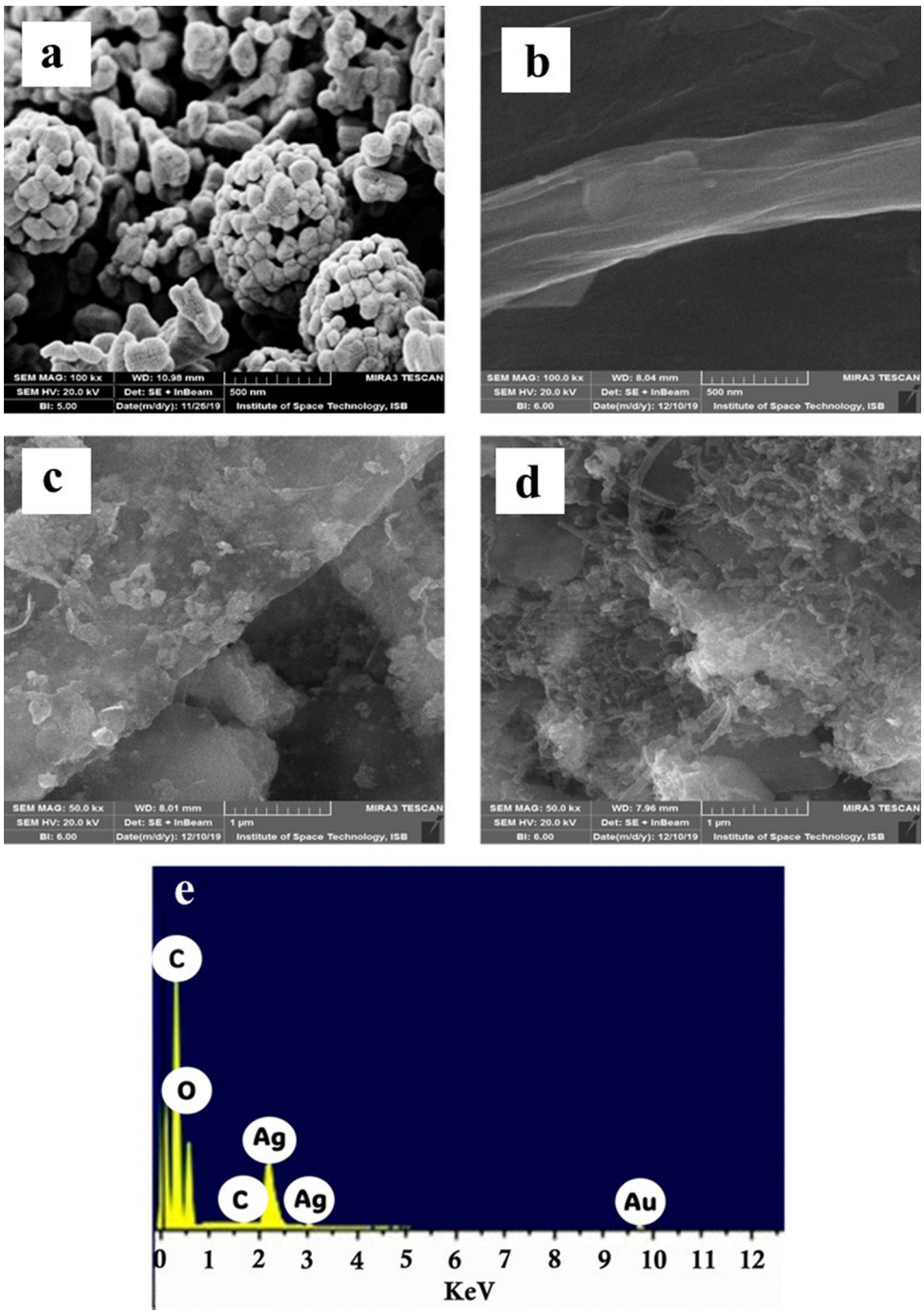

Fig. 4 SEM images of (a) Ag NPs, (b) rGO, (c) Ag@rGO and (d) Ag@rGO/CNT, and (e) EDX graph of Ag@GO/CNT.

extended periods. Its stability in aqueous solutions can be enhanced by adding stabilizers, such as NaOH, which prevents premature hydrolysis.[70] The hydrolysis of $NaBH_4$ produces hydrogen of high purity, which is essential for fuel cell applications.[69] In addition, unlike some other hydrogen production methods that require high temperatures or pressures, $NaBH_4$ hydrolysis occurs under mild conditions, making the process more energy-efficient and safer. Finally, although currently challenging and costly, there is potential for regenerating $NaBH_4$ from its by-products, which could enhance the sustainability of this hydrogen production method in the future.[70] A tabulated form of the comparison between $NaBH_4$ hydrolysis and other H_2 sources is given in Table 3.

3.8. Cost-effectiveness of the process and commercialization

Currently, $NaBH_4$ is not cost-competitive compared to other hydrogen production methods. It remains an attractive option for specialized applications, such as portable fuel cells (*e.g.*, military, aerospace, emergency power) and hydrogen storage, where safety and transportability are crucial. If breakthroughs

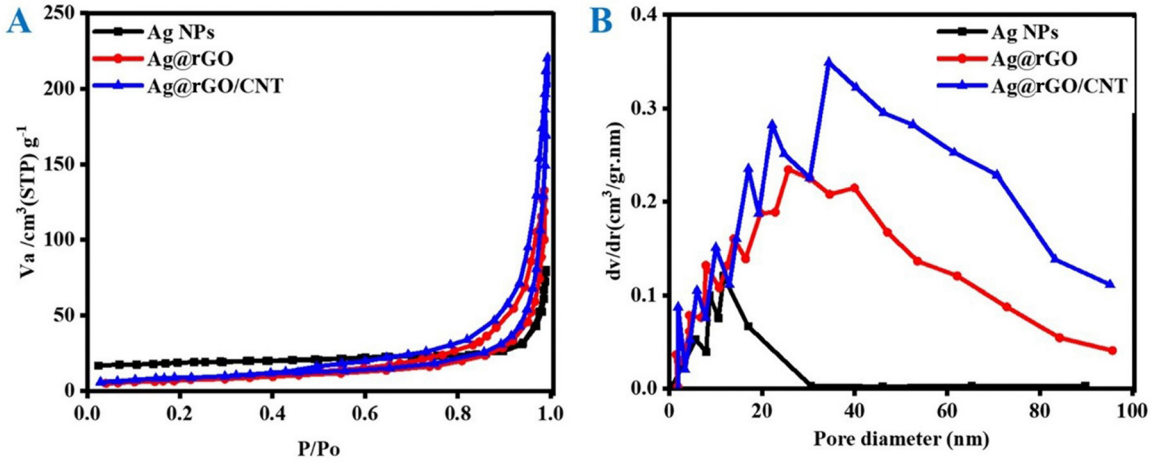

Fig. 5 (A) The isotherm of nitrogen adsorption–desorption and (B) distribution curves of BJH pore sizes for Ag NPs, Ag@rGO, and Ag@rGO/CNT catalysts.

Table 3 Comparison of $NaBH_4$ with other H_2 sources

Method	Energy requirement	Safety	Carbon emissions	Storage & transport	On-demand H_2 release
$NaBH_4$ hydrolysis	Low	High (stable solid)	None	Easy (solid material)	Yes (controlled)
Steam methane reforming (SMR)	High (700–1100 °C)	Moderate (flammable gas)	High (CO_2 emissions)	Difficult (compressed H_2)	No
Water electrolysis	High (electricity required)	High	None (if using renewable energy)	Difficult (compressed H_2)	No
Metal hydrides	Moderate	High	None	Moderate	Yes (slow release)

in low-cost production and recycling occur, $NaBH_4$ could become a viable alternative for widespread hydrogen use. Furthermore, large-scale production could reduce per-unit costs through economies of scale. $NaBH_4$ hydrolysis is not yet widely commercialized for large-scale hydrogen production. Still, it is used in niche applications, including military fuel cells, backup power systems, aerospace applications, and remote hydrogen supply for field operations. Some prototype hydrogen-powered cars and UAVs have used $NaBH_4$ as a hydrogen source.

3.9. Catalytic hydrogen generation in the presence of $NaBH_4$

Using the popular water displacement method, the amount of hydrogen generated on the catalysts' surface due to the hydrolysis of $NaBH_4$ was continually evaluated to assess the effectiveness of the catalysts created in the sodium borohydride hydrolysis process.

The hydrolysis of $NaBH_4$ is known to produce hydrogen exothermically, spontaneously, and without external intervention. $NaBH_4$ is an excellent material for hydrogen fuel storage due to its high concentration of hydrogen ions (10.8%), stability, accessibility, and environmental acceptability. Without a catalyst, spontaneous hydrolysis proceeds so slowly that it takes more than a day to produce a minimal amount of hydrogen, even in the presence of abundant water. By using the right catalyst and water, $NaBH_4$ gets hydrolyzed to yield around 4 moles of hydrogen (eqn (1)).

$$NaBH_4 \rightarrow 4H_2 + NaBO_2 \quad (1)$$

The results of the hydrolysis of $NaBH_4$ by the prepared samples (Ag NPs, Ag@rGO, Ag@rGO/CNT) are given in Fig. 6A. The results show that the maximum hydrogen is produced by the Ag@rGO/CNT catalyst. The high performance of Ag@rGO/CNT is obviously due to the introduction of CNT to the Ag@rGO composite. This may be because the CNTs significantly enhance the material's electrical conductivity due to their high intrinsic conductivity and large surface area, allowing for better dispersion and attachment of silver nanoparticles, thereby improving the overall electrical performance of Ag@rGO/CNT. The Ag@rGO/CNT's exceptional catalytic activity achieved a maximum generation rate of 4243 mL min^{-1} $g_{cat}{}^{-1}$. On the other hand, Ag NPs and Ag@rGO do not perform as well due to their poor particle dispersion and pore properties. Specifically, the samples' pore volume agrees with the outcomes. Therefore, Ag@rGO/CNT was selected as the primary catalyst for the hydrolysis process, allowing for further investigation to be carried out.

However, the sodium borohydride hydrolysis process was carried out at 25 °C with 25 mg of catalyst and a 5 mL solution containing 50 mg of $NaBH_4$, separately in both continuous and batch configurations, to assess the effect of reactor setup type on the hydrogen generation rate. In the batch reactor, water was added to a catalyst and $NaBH_4$ mixture. In contrast, the continuous reactor utilized a syringe pump with a fixed $NaBH_4$ flow rate. This was the only difference between the two approaches. Fig. 6B illustrates that the batch system generated more hydrogen in a shorter time. The constant system produced 211 mL of

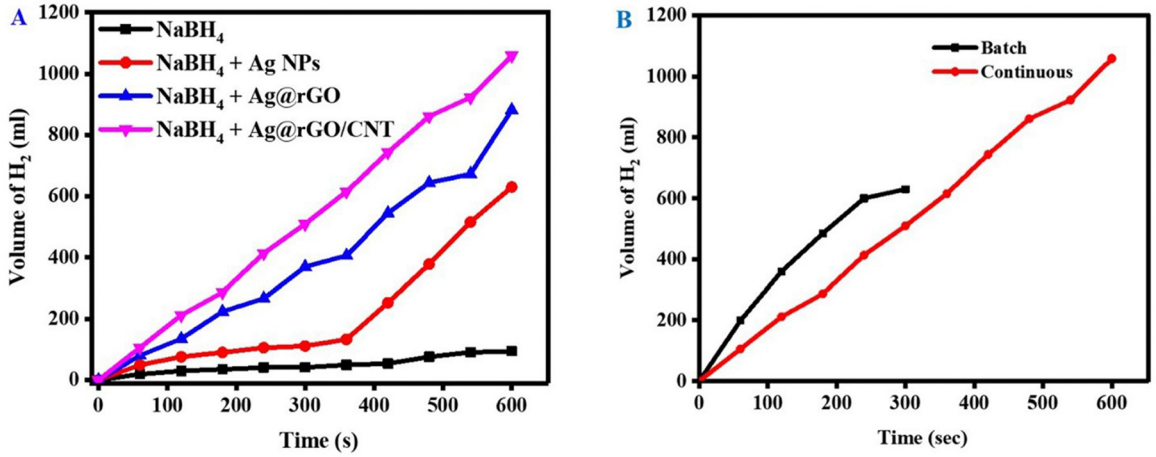

Fig. 6 (A) Time-dependent plot for the hydrolysis of $NaBH_4$ catalyzed by Ag NPs, Ag@rGO and Ag@rGO/CNT, and in the absence of a catalyst. (B) Comparison of hydrogen development in batch and continuous systems during $NaBH_4$ hydrolysis.

H_2 in 2 minutes, whereas the batch produced 360 mL. The fact that the reactants are constantly supplied in a continuous flow reactor, whereas they are provided all at once in a batch reactor, is why they end earlier than continuous reactors. In a batch reactor, the reaction may stop too soon if a reactant is used up before it is finished. The yield can also be increased by the batch setup's greater exposure of the borohydride ion to the catalytic active sites. Despite this, the absence of thorough studies on the hydrolysis process of sodium borohydride and its related parameters in continuous systems prompted hydrogen production to be carried out in a continuous stirred tank reactor to advance the research.

3.10. Effect of different parameters on the catalyst activity

In our continuous experiment, $NaBH_4$ was added to the catalyst and water to initiate the catalytic process. The amount of hydrogen produced during the conversion of sodium borohydride over time under ambient conditions was calculated using the water displacement method. In hydrogen generation, turnover frequency (TOF) is a crucial metric that indicates the intrinsic activity of a catalyst. It signifies the number of hydrogen molecules that can be produced per active site on the catalyst per unit of time, essentially measuring the catalyst's efficiency in converting reactants into hydrogen. This makes it a key factor in evaluating and comparing different catalysts for hydrogen production. Compared with Ag NPs and Ag@rGO, the Ag@rGO/CNT catalyst has a high TOF value, as seen in Fig. 7A. Eqn (2) was applied to determine the catalytic efficiency based on the catalyst's synthesized turnover frequency (TOF).[71]

$$\mathrm{TOF} = \frac{\text{volume of hydrogen production}}{\text{weight of used catalyst} \times \text{time}} \qquad (2)$$

As shown in Fig. 7A, the TOF of the prepared catalysts shows that the Ag@rGO/CNT catalyst has a high TOF towards hydrogen production compared to other catalysts. The CNT increases the surface area and reactivity of the Ag@rGO/CNT catalyst, which could be the basis. In addition, the Ag@rGO/CNT nanocomposite TOF was comparable to other previously characterized catalysts for hydrogen production.

3.10.1. Effect of $NaBH_4$ loading. Several experiments were done to determine the effect of $NaBH_4$ addition on hydrogen production while keeping other experimental parameters constant. Fig. 7B shows that when $NaBH_4$ is loaded, hydrogen generation rises almost linearly. Therefore, gradually adding $NaBH_4$ is an effective method for producing the desired hydrogen output. It can also be observed that. During solution injection, hydrogen creation shows a steady rate at a constant flow rate.

3.10.2. Effect of catalyst loading. Fig. 7C illustrates how the amount of hydrogen gas generated depends on the dosage of the catalyst. The hydrogen produced rose when the catalyst was raised from 15 to 25 mg. However, after this, when the catalyst dosage was raised to 50 mg, the hydrogen generation rate began to drop. This is because although adding more catalysts results in more catalytically active sites, it also makes the solution more viscous, which increases the coverage of active sites and lowers the amount of hydrogen produced.[5] It can be concluded, therefore, that the increase in hydrogen production during the early phases of the process was primarily due to the increase in catalytic active sites. However, mass transfer barriers cause a decrease in hydrogen production when the catalyst dosage exceeds 25 mg.

3.10.3. Effect of increasing pH. Keeping other experimental parameters constant, numerous tests were conducted to investigate the effect of a basic solution (NaOH) on hydrogen production (Fig. 7D). $NaBH_4$ hydrolysis occurs when a hydronium ion contacts a borohydride anion in an acidic environment. A decrease in the hydrolysis of $NaBH_4$ results in a reduction in proton concentration, which in turn leads to a decline in the rate of hydrogen synthesis in an alkaline solution (NaOH). Using the Ag@rGO/CNT catalyst, four experiments were conducted to examine the NaOH concentration (0, 10^{-2}, 10^{-4}, 10^{-6} M) effect on $NaBH_4$ hydrolysis at R.T. As shown in Fig. 7D, hydrogen production slowly decreased as the NaOH concentration rose. Therefore, the concentration of basic and acidic solutions has a significant influence on hydrogen generation.

3.10.4. The impact of feed flow rate. Fig. 8A illustrates how the flow of a reactive solution influences the hydrogen

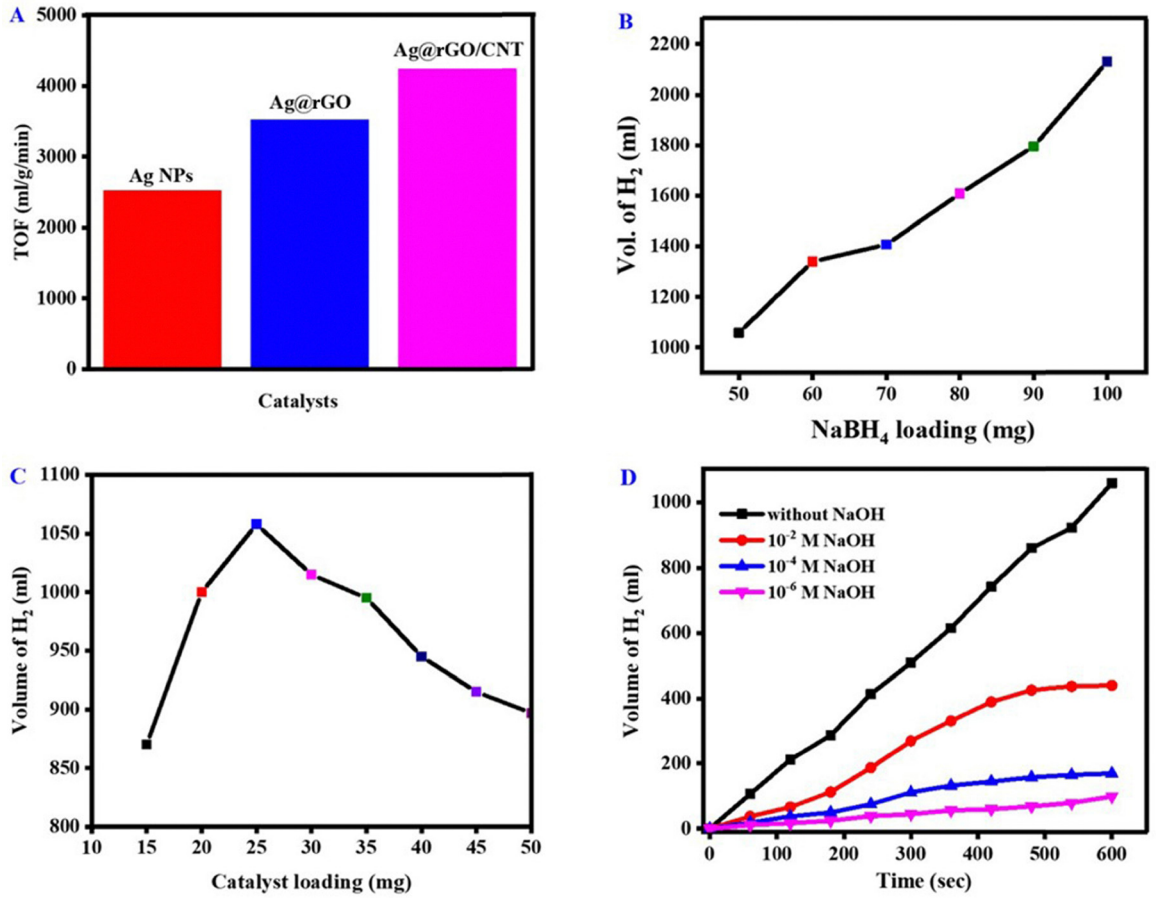

Fig. 7 (A) Turnover frequency in the presence of Ag NPs, Ag@rGO, and Ag@rGO/CNT, (B) effect of $NaBH_4$ loading, (C) effect of catalyst loading on hydrogen production in the presence of Ag@rGO/CNT, (D) effect of NaOH concentration on hydrogen production in the presence of Ag@rGO/CNT.

generation rate of a continuous system. The findings show that the volume of hydrogen produced decreases with increasing flow rates due to the solution's increased viscosity and active site coverage, resulting in a less significant reaction. Additionally, during solution injection, it is evident that hydrogen creation occurs at a steady pace with a continuously low flow rate.

3.10.5. The impact of temperature. A range of temperature (25–40 °C) was used in the tests to examine the effects of temperature on the catalytic hydrolysis of sodium borohydride while keeping the concentrations of sodium hydroxide, catalyst, and sodium borohydride constant. The findings, as shown in Fig. 8B, indicate that the temperature and reaction rate in the sodium borohydride hydrolysis process are directly correlated, resulting in increased hydrogen generation. Since molecules are more accessible and active at higher temperatures, a higher temperature is beneficial for achieving a faster hydrogen generation rate.

3.10.6. Kinetic study. The hydrolysis of $NaBH_4$ exhibits zero-order kinetics, as illustrated in Fig. 8C. According to numerous reports in the literature.[72] This is the foundation for the finding that the amount of hydrogen produced increases linearly over time at fixed $NaBH_4$ concentrations. Thus, the kinetic study uses zero-order reaction computation. Eqn (3) and (4) of the Arrhenius equation can be used to compute the activation energy by calculating the slope of the resulting line:

$$r = k = k_0 \cdot \exp\left(-\frac{E_a}{RT}\right) \quad (3)$$

$$\ln(r) = \ln(k_0) - \frac{E_a}{RT} \quad (4)$$

In the equations above, "r" represents the rate at which hydrogen is generated, "k_0" denotes the frequency factor, "E_a" means the activation energy, "R" represents the ideal gas constant, and "T" represents the reaction temperature.

Based on the data in Fig. 8B, the correlation between $\ln k$ and $1/T$ is visually displayed in Fig. 8C. The resulting line's slope indicated that the activation energy of the Ag@rGO/CNT catalyst was 7.08 kJ mol^{-1}. However, the activation energy for additional catalysts was also calculated. With a lower activation energy, reaction rates are usually faster and can be facilitated more successfully. Additionally, the reported activation energy values match the pore characteristics of the catalysts. The relatively low activation energy of Ag@rGO/CNT facilitates the catalyst by reducing the energy required to initiate the reaction.

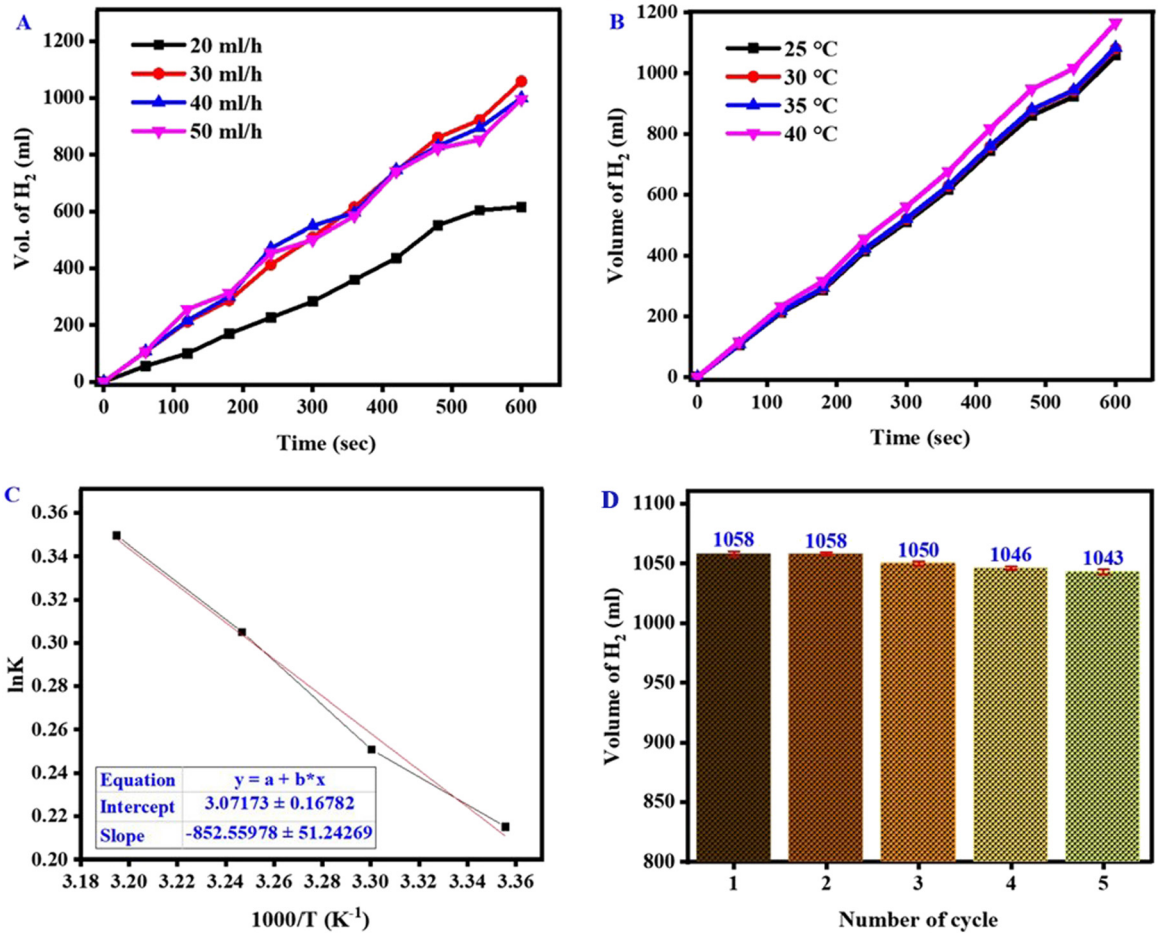

Fig. 8 (A) The impact of the $NaBH_4$ flow rate on hydrogen production, (B) the relationship between temperature and hydrogen production, (C) Arrhenius diagram generated using the information in Fig. 8, and (D) the stability of the Ag@rGO/CNT catalyst over 4 repetitive cycles.

3.10.7. Mechanism of sodium borohydride hydrolysis to produce hydrogen. The process for determining hydrogen evolution using sodium borohydride hydrolysis (hydride hydrolysis) was described by Santos and Sequeira.[73] The basis of this technique is the gasometric detection of hydrogen development upon BH^- hydrolysis. In contrast to traditional hydrogen evolution techniques (Fig. S1, ESI†), the apparatus employed in this case is more straightforward and less complex, and essentially, it does not require temperature or pressure control throughout the measurement procedure. The hydrogen is produced when sodium borohydride undergoes hydrolysis in the presence of a catalyst.[5] The formation of MH is caused by reversible adsorption and desorption surface interactions of borohydride (eqn (5)). In the following stages, one electron is released, forming borane (BH_3) (eqn (6)). As eqn (7) indicates, borane can then combine with an OH^- anion to generate a stable intermediate ion (BH_3OH^-). Following similar procedures, the stable intermediate can create $B(OH)^-$ (eqn (5)–(9)). Hydrogen can be produced by hydrolysis of BH^- (eqn (8)) in the presence of a catalyst. Silver's synergistic impact and enhancement of the active surface center are the primary causes of the Ag@rGO/CNT catalyst's increased hydrolysis activity, resulting in the creation of additional hydrogen.

$$2M + BH_4^- \leftrightarrow MBH_3^- + MH \quad (5)$$

$$MBH_3^- \leftrightarrow BH_3 + M + e^- \quad (6)$$

$$M + e^- + H_2O \rightarrow MH + OH^- \quad (7)$$

$$BH_3 + OH^- \rightarrow BH_3OH^- \quad (8)$$

$$MH + MH \rightarrow H_2 + 2M \quad (9)$$

3.10.8. Reusability test. The catalyst's stability is crucial for the successful commercialization of hydrogen-generating systems that rely on the hydrolysis of $NaBH_4$. The current study evaluated the catalytic stability of the Ag@rGO/CNT catalyst through four consecutive and repeated applications. The results show that the catalyst's activity declines with each additional application, as seen in Fig. 8D. A significant portion of the catalyst activity drop is attributed to the leaching of the silver active phase and the corresponding decrease in catalyst mass that occurs with each wash. Other reasons exist for reducing catalyst activity, such as the metal active phase aggregating or byproducts building up on the catalyst surface. On a brief note, it is well understood that metal nanoparticles (*e.g.*, Ag, Pt) are initially dispersed on a support material (*e.g.*, carbon, metal oxides). Over time, these nanoparticles coalesce into larger clusters through a process known as sintering. This

reduces the active surface area, leading to lower catalytic efficiency. This results in fewer active sites for $NaBH_4$ hydrolysis, reduced reaction rate, and catalyst deactivation.[74]

Secondly, the hydrolysis of $NaBH_4$ produces sodium metaborate ($NaBO_2$) as a by-product. Over time, $NaBO_2$ accumulates on the catalyst surface, forming a passivation layer. This blocks active sites, preventing further hydrogen generation. If the by-product layer is too thick, the catalyst may become permanently inactive. It is also possible that silver may undergo oxidation or other chemical modifications in water-based systems. This alters their electronic properties, reducing their catalytic efficiency. Once metal nanoparticles aggregate, the active surface area shrinks, leading to faster $NaBO_2$ buildup on the remaining active sites and accelerating catalyst deactivation.[75–77]

4. Conclusions

This study highlights the successful phyto-mechanochemical reduction of silver and graphene oxide to form silver nanoparticles (AgNPs) and silver-reduced graphene oxide (Ag@rGO). To produce hydrogen as efficiently as possible by the hydrolysis of sodium borohydride ($NaBH_4$) in a continuous flow system, these materials have been coupled with carbon nanotubes (CNTs). The water displacement method was employed to assess the hydrolysis of $NaBH_4$ at 25 °C, using 25 mg of catalyst and 5 mL of an aqueous solution containing 50 mg of $NaBH_4$. Ag@rGO/CNT was found to possess exceptional properties, resulting in a high hydrogen generation rate of 4243 mL min^{-1} $g_{cat}{}^{-1}$. Ag@GO exhibits more activity than Ag NPs due to its larger surface area, higher particle distribution, and enhanced electrical conductivity. Furthermore, it was found that the activation energy was lower than the others, reaching as low as 7.08 kJ mol^{-1}. When designing and utilizing this catalyst in the sodium borohydride hydrolysis process, its low activation energy is considered favourable. However, the Ag@GO/CNT catalyst's catalytic activity gradually decreased over four successive applications. This behaviour was attributed mainly to the decrease in catalyst mass during each phase. A noteworthy strategy for promoting phyto-mechanochemical reactions through the deliberate selection of carbon-based catalysts is highlighted in this work.

Author contributions

Fatimah Al-Sulami: writing – original draft, investigation; Merfat M. Alsabban, Hadeel M. Banbela; Aysha Afzal: methodology, formal analysis; Noushi Zaidi, Sadaf Habib, Dina Hajjar, Arwa A Makki, Ismat Bibi, Tariq Javed: data curation; Muhammad Babar Taj: supervision, visualization; writing – review & editing, project administration.

Data availability

The data will be available upon request from the corresponding author.

Conflicts of interest

The authors declare no conflicts of interest.

Acknowledgements

The authors acknowledge support from the University of Jeddah, Saudi Arabia; the Higher Education Commission, Pakistan; and King Faisal University, Saudi Arabia.

References

1 I. Maseeh, F. Anwar, S. Aroob, T. Javed, I. Bibi, A. Almasoudi, A. Raheel, M. A. Javid, S. A. Carabineiro and M. B. Taj, *Mater. Adv.*, 2024, **5**, 5080–5095.
2 S. Schwarz, G. Daurer, B. Plank, H.-G. Krull, A. Szittnick, M. A. Lakhdari, S. Collin, P. Gasca, E. Chauveau and C. Deville-Cavellin, *Int. J. Hydrogen Energy*, 2025, **101**, 1105–1115.
3 A. Paudel and J.-K. Choi, *Int. J. Hydrogen Energy*, 2025, **98**, 295–307.
4 K. C. Mandal, T. Das and B. K. Das, *Int. J. Green Energy*, 2025, 1–26.
5 W. Raza, K. Ahmad and H. Kim, *Nanotechnology*, 2021, **32**, 495404.
6 R. Guduru, R. Singh, R. Patel and R. K. Vij, *Subsurface Hydrogen Energy Storage*, Elsevier, 2025, pp. 31–61.
7 A. Bhardwaj and V. K. Singh, *Renewable Energy Development: Technology, Material and Sustainability*, Springer, 2025, pp. 25–42.
8 A. O. Maka, M. Mehmood and T. N. Chaudhary, *Clean Energy*, 2025, zkae106.
9 N. Dyantyi-Gwanya, S. O. Giwa, T. Ncanywa and R. T. Taziwa, *Sustainability*, 2025, **17**, 901.
10 Ü. Ecer, A. Zengin and T. Şahan, *J. Energy Inst.*, 2025, 101974.
11 S. Jana, A. Parthiban and W. Rusli, *Chem. Commun.*, 2025, **61**, 3233–3249.
12 N. E. Toprak, G. Bozkurt and A. Özer, *Int. J. Hydrogen Energy*, 2025, **103**, 232–240.
13 S. Li, S. Qiu, Y. S. Chua, Y. Xia, Y. Zou, F. Xu, L. Sun and H. Chu, *Mater. Chem. Phys.*, 2024, **319**, 129399.
14 X. Xu, H. Yong, Y. Zhao, S. Wang, K. Feng, Y. Wang, B. Liu, J. Hu and Y. Zhang, *Mater. Charact.*, 2024, **210**, 113821.
15 C. Luo, S. Liu, Y. Wang, J. Hu, E. Lester and T. Wu, *Energy*, 2024, **306**, 132341.
16 S. X. Chin, J. Vincent, N. F. Razak, N. Daud, S. Chowdhury, C. Wongchoosuk and C. H. Chia, *J. Renewable Sustainable Energy*, 2025, **17**(2), 938–951.
17 E. Onat, S. Ekinci, Ö. Şahin and M. S. Izgi, *Int. J. Hydrogen Energy*, 2025, DOI: **10.1016/j.ijhydene.2025.01.073**.
18 D. Xue, B. Yi, Y. Wan, Y. Yan, D. Chai and G. Li, *Energy Fuels*, 2025, **39**, 2555–2567.
19 Y. Yu, Z. Qin, X. Zhang, Y. Chen, G. Qin and S. Li, *ACS Mater. Lett.*, 2025, **7**, 319–332.
20 K. Zhang, L. L. Zhang, X. Zhao and J. Wu, *Chem. Mater.*, 2010, **22**, 1392–1401.
21 S.-M. Paek, E. Yoo and I. Honma, *Nano Lett.*, 2008, **9**, 72–75.

22 L. Dong, R. R. S. Gari, Z. Li, M. M. Craig and S. Hou, *Carbon*, 2010, **48**, 781–787.
23 Y. Gründer, M. D. Fabian, S. G. Booth, D. Plana, D. J. Fermín, P. I. Hill and R. A. Dryfe, *Electrochim. Acta*, 2013, **110**, 809–815.
24 R. R. Nayak, H. S. Khairun, G. Parveen, A. Garg, Y. Chumachenko, R. Shu and N. K. Gupta, *Chem. - Asian J.*, 2025, **20**, e202401005.
25 M. A. Afzal, M. Javed, S. Aroob, T. Javed, M. M. Alnoman, W. Alelwani, I. Bibi, M. Sharif, M. Saleem and M. Rizwan, *Nanomaterials*, 2023, **13**, 2079.
26 S. Javaid, M. S. Khan, M. B. Taj, H. Afzal, I. Batool, A. Almasoudi, M. Ghaznavi, T. Javed, S. Qureshi and W. Azeem, *Int. J. Environ. Anal. Chem.*, 2024, 1–31.
27 F. Ahmad, M. B. Taj, M. Ramzan, A. Raheel, S. Shabbir, M. Imran and H. M. Iqbal, *Mater. Res. Express*, 2020, **7**, 015026.
28 W. Alelwani, M. B. Taj, R. M. Algheshairy, A. M. Alnajeebi, H. F. Alharbi, A. M. Bannunah, A. H. Habib, A. Raheel, S. Shabbir and R. H. Ahmad, *Chem. Afr.*, 2022, **5**, 1527–1543.
29 F. Ahmad, M. B. Taj, M. Ramzan, H. Ali, A. Ali, M. Adeel, H. M. Iqbal and M. Imran, *J. Nanostruct. Chem.*, 2021, **11**, 131–141.
30 M. Usman, M. B. Taj and S. A. C. Carabineiro, *Environ. Sci. Pollut. Res.*, 2023, **30**, 102027.
31 A. Jabbar, A. Abbas, N. Assad, M. Naeem-ul-Hassan, H. A. Alhazmi, A. Najmi, K. Zoghebi, M. Al Bratty, A. Hanbashi and H. M. Amin, *RSC Adv.*, 2023, **13**, 28666–28675.
32 N. Assad, M. Naeem-ul-Hassan, M. Ajaz Hussain, A. Abbas, M. Sher, G. Muhammad, Y. Assad and M. Farid-ul-Haq, *Nat. Prod. Res.*, 2023, 1–15.
33 S. Ullah, R. Khalid, M. F. Rehman, M. I. Irfan, A. Abbas, A. Alhoshani, F. Anwar and H. M. Amin, *Front. Chem.*, 2023, **11**, 1202252.
34 M. Awan, S. Rauf, A. Abbas, M. H. Nawaz, C. Yang, S. A. Shahid, N. Amin and A. Hayat, *J. Mol. Liq.*, 2020, **317**, 114014.
35 L. Perini, C. Durante, M. Favaro, S. Agnoli, G. Granozzi and A. Gennaro, *Appl. Catal., B*, 2014, **144**, 300–307.
36 X. Gao, J. Wang, Z. Ma and J. Ye, *Electrochim. Acta*, 2014, **130**, 543–550.
37 D. R. Dreyer, S. Park, C. W. Bielawski and R. S. Ruoff, *Chem. Soc. Rev.*, 2010, **39**, 228–240.
38 G. Eda and M. Chhowalla, *Adv. Mater.*, 2010, **22**, 2392–2415.
39 S. Ratso, I. Kruusenberg, M. Vikkisk, U. Joost, E. Shulga, I. Kink, T. Kallio and K. Tammeveski, *Carbon*, 2014, **73**, 361–370.
40 Y. Yan, J. Miao, Z. Yang, F.-X. Xiao, H. B. Yang, B. Liu and Y. Yang, *Chem. Soc. Rev.*, 2015, **44**, 3295–3346.
41 J. Li, M. Moskovits and T. L. Haslett, *Chem. Mater.*, 1998, **10**, 1963–1967.
42 E. Hutter and J. H. Fendler, *Adv. Mater.*, 2004, **16**, 1685–1706.
43 S. Aroob, M. B. Taj, S. Shabbir, M. Imran, R. H. Ahmad, S. Habib, A. Raheel, M. N. Akhtar, M. Ashfaq and M. Sillanpää, *J. Environ. Chem. Eng.*, 2021, **9**, 105590.
44 M. B. Taj, M. D. Alkahtani, A. Raheel, S. Shabbir, R. Fatima, S. Aroob, R. Yahya, W. Alelwani, N. Alahmadi and M. Abualnaja, *Sci. Rep.*, 2021, **11**, 5439.
45 Z. Irshad, S. Javaid, O. M. Ali, M. S. Khan, F. M. H. AlSulami, A. Almasoudi, A. A. Al-Ghamdi, H. M. Banbela, D. Hajjar and A. A. Makki, *ChemistrySelect*, 2025, **10**, e202405145.
46 L. Shahriary, R. Nair, S. Sabharwal and A. A. Athawale, *New J. Chem.*, 2015, **39**, 4583–4590.
47 F.-Y. Kong, W.-W. Li, J.-Y. Wang and W. Wang, *Biosens. Bioelectron.*, 2015, **69**, 206–212.
48 N. Meng, S. Zhang, Y. Zhou, W. Nie and P. Chen, *RSC Adv.*, 2015, **5**, 70968–70971.
49 B. Fan, Y. Li, F. Han, T. Su, J. Li and R. Zhang, *J. Mater. Sci.: Mater. Med.*, 2018, **29**, 1–9.
50 N. T. Lan, N. X. Dinh, N. D. Hung, H. Lan, P. A. Tuan, L. H. Thang, N. N. Trung, N. Q. Hoa, T. Q. Huy and N. Van Quy, *J. Alloys Compd.*, 2014, **615**, 843–848.
51 M. R. Islam, M. Ferdous, M. I. Sujan, X. Mao, H. Zeng and M. S. Azam, *J. Colloid Interface Sci.*, 2020, **562**, 52–62.
52 L. Huang, H. Yang, Y. Zhang and W. Xiao, *J. Nanomater.*, 2016, **2016**, 5685967.
53 Y. Guo, X. Yang, K. Ruan, J. Kong, M. Dong, J. Zhang, J. Gu and Z. Guo, *ACS Appl. Mater. Interfaces*, 2019, **11**, 25465–25473.
54 M. Adil, S. Alam, U. Amin, I. Ullah, M. Muhammad, M. Ullah, A. Rehman and T. Khan, *AMB Express*, 2023, **13**, 115.
55 N. Sabapathi, S. Ramalingam, K. N. Aruljothi, J. Lee and S. Barathi, *Plants*, 2023, **12**, 707.
56 N. Shanmugam, P. Rajkamal, S. Cholan, N. Kannadasan, K. Sathishkumar, G. Viruthagiri and A. Sundaramanickam, *Appl. Nanosci.*, 2014, **4**, 881–888.
57 K. Mandal, D. Das, S. K. Bose, A. Chaudhuri, A. Chakraborty, S. Mandal, S. Ghosh and S. Roy, *Sci. Rep.*, 2024, **14**, 31174.
58 M. M. Aljeldah, M. T. Yassin, A. A.-F. Mostafa and M. A. Aboul-Soud, *Infect. Drug Resist.*, 2023, 125–142.
59 A. L. Widyaningtyas, Y. Yulizar and D. O. B. Apriandanu, *IOP Conf. Ser.:Mater. Sci. Eng.*, 2019, **509**, 012022.
60 N. Gao, Y. Chen and J. Jiang, *ACS Appl. Mater. Interfaces*, 2013, **5**, 11307–11314.
61 M. Vanaja, K. Paulkumar, M. Baburaja, S. Rajeshkumar, G. Gnanajobitha, C. Malarkodi, M. Sivakavinesan and G. Annadurai, *Bioinorg. Chem. Appl.*, 2014, 742346.
62 J. Chen, X. Zheng, H. Wang and W. Zheng, *Thin Solid Films*, 2011, **520**, 179–185.
63 Y. Y. Loo, B. W. Chieng, M. Nishibuchi and S. Radu, *Int. J. Nanomed.*, 2012, **7**, 4263.
64 A. Monshi, M. R. Foroughi and M. R. Monshi, *World J. Nano Sci. Eng.*, 2012, **2**, 154–160.
65 J. Yang, C. Zang, L. Sun, N. Zhao and X. Cheng, *Mater. Chem. Phys.*, 2011, **129**, 270–274.
66 N. Belachew, D. S. Meshesha and K. Basavaiah, *RSC Adv.*, 2019, **9**, 39264–39271.
67 Y. Yang, H. Shen, J. Yang, K. Gao, Z. Wang and L. Sun, *RSC Adv.*, 2022, **12**, 19144–19153.
68 D. Kumar, S. Nain, H. Pal and R. Kumar, *Nanosci. Nanotechnol.*, 2016, **6**(3), 39–42.
69 S. Gurdal, *Molecules*, 2024, **29**, 4893.
70 U. B. Demirci and P. Miele, *Energy Environ. Sci.*, 2009, **2**, 627–637.
71 S. Ullah, M. Shaban, A. B. Siddique, A. Zulfiqar, N. S. Lali, M. Naeem-ul-Hassan, M. I. Irfan, M. Sher, M. F. ur

Rehman and A. Hanbashi, *J. Environ. Chem. Eng.*, 2024, **12**, 113350.
72 H.-B. Dai, Y. Liang, L.-P. Ma and P. Wang, *J. Phys. Chem. C*, 2008, **112**, 15886–15892.
73 D. Santos and C. Sequeira, *Int. J. Hydrogen Energy*, 2010, **35**, 9851–9861.
74 A. van Hoof, R. van der Poll, H. Friedrich and E. Hensen, *Appl. Catal., B*, 2020, **272**, 118983.
75 Y. Shang, Loughborough University, 2007.
76 C. R. Cloutier, University of British Columbia, 2006.
77 H. X. Nunes, D. L. Silva, C. M. Rangel and A. M. Pinto, *Energies*, 2021, **14**, 3567.